Optimizing Wettability of Externally Wetted Microfabricated Silicon Electrospray Thrusters

by

Tanya Cruz Garza

S.B., Aerospace Engineering, Massachusetts Institute of Technology, 2004

Submitted to the Department of Aeronautics and Astronautics
in partial fulfillment of the requirements for the degree of

Master of Science

at the

MASSACHUSETTS INSTITUTE OF TECHNOLOGY

January 2007

Author .....
Department of Aeronautics and Astronautics
January 19, 2007

Certified by .....
Manuel Martínez-Sánchez
Professor of Aeronautics and Astronautics
Thesis Supervisor

Accepted by .....
Jaime Peraire
Chair, Committee on Graduate Students

Optimizing Wettability of Externally Wetted Microfabricated Silicon Electrospray Thrusters

by

Tanya Cruz Garza

Submitted to the Department of Aeronautics and Astronautics
on January 19, 2007, in partial fulfillment of the
requirements for the degree of
Master of Science

Abstract

Electrospray propulsion devices with externally wetted architectures have shown favorable performance. The design of microfabricated silicon thrusters and their feed systems requires an understanding of propellant flow over a silicon surface. This research explores the parameters that affect wettability of externally wetted microfabricated silicon electrospray thruster arrays and how varied wetting surface treatments affect thruster performance.

Silicon samples with various black silicon treatments were fabricated and optimal black silicon etch parameters were determined by measuring the samples wettability. Silicon wettability was analyzed by producing samples with various black silicon treatments and then measuring contact angle, measuring surface roughness, imaging surface geometry, calculating spreading rates, and performing treated thruster current output tests. Two propellants, 1-ethyl-3-methyl-imidazolium tetraflouroborate (EMI-BF_4) and 1-ethyl-3-methyl-imidazolium bis(triflouromethyl-sulfonyl)amide (EMI-IM), were used in contact angle measurements and spreading rate experiments.

A model describing the spread of a small drop of EMI-BF_4 and EMI-IM over roughened silicon substrates is presented. Models which describe the spread of small, non-reactive drops over perfectly smooth substrates predicts a 1/5th power dependence of spreading area with time. Experimental spreading data of EMI-BF_4 loosely supported this theory showing an average of 1/3rd power dependence of spread area with time. A model of propellant spreading is proposed here suggesting that viscous spreading reaches an equilibrium with constant radius and provides a capillary pressure source for porous flow through the black silicon surface for the remainder of the spreading. This theory is compared with experimental data of EMI-BF_4 and EMI-IM propellant spread over roughened silicon.

Future work in propellant supply to a thruster surface is discussed. Theoretical and experimental areas of study are proposed to understand physical flow mechanisms involved in electrospray thrusters.

Thesis Supervisor: Manuel Martínez-Sánchez
Title: Professor of Aeronautics and Astronautics

Acknowledgments

Funding for this project was provided by the US Air Force Office of scientific Research (AFOSR), Mitat Birkan technical monitor, Darpa, MGA program, Clark Nguyen project manager, the GEM Fellowship, the Lemelson Minority Engineering Fellowship, and the MIT Aeronautics and Astronautics Department.

I would like to thank Liang-Yu Chen for her help obtaining high resolution Scanning Electron Microscope (SEM) images, Blaise Gassend for providing thrusters to test, and Selim Sumer for fabricating a testing device to hold the emitters.

I would like to thank Prof. Martínez-Sánchez for his intellectual and professional guidance as well as Professor Tayo Akinwande, Luis F. Velásquez-García for providing his microfabrication expertise and general guidance, and Paulo Lozano for his advise on experimental testing.

I would like to thank the students of the Microsystems Technologies Lab willingness to help. The author would like to thank Space Propulsion Lab students Murat, Felix, Justin, Justin, Mike, Ben, Shannon, Yassir, Noah, Nareg, Jean Marie, Jorge, Tim, Bobby, Dan, and Chris for their friendship and for making my experience in this lab an interesting one.

Finally, I would like to thank my mother Sylvia and my father Cayetano for giving me my faith and values and for their endless support and love.

Contents

List of Figures

List of Tables

Chapter 1

Introduction

Externally wetted silicon electrospray thrusters are devices which produce low thrusts and high velocity increases for spacecraft. The surface of such a thruster must allow propellant to spread evenly and to move freely in response to electric traction forces applied to it. A surface treatment for silicon is found which produces a completely wettable silicon surface and an analytical model describing the spread of propellant over a dry silicon surface with nanometer scale roughness is presented and compared with experiment.

Chapter two describes the processing done to produce various rough, wettable silicon surfaces otherwise known as black silicon.

Chapter three describes the methods for measuring and testing the wettability of the black silicon treatments. These experiments offer a basis of comparison between the treatments for determining an optimal treatment.

Chapter four outlines an analytical model which describes spread of a small, non-reactive propellant drop of either EMI-BF_4 or EMI-IM over a flat black silicon surface.

Chapter five determines the optimal black silicon treatment based on wetting measurements and compares the spreading model from chapter 4 with experimental results from section 3.4.

Chapter six makes concluding remarks and discusses recommendations for future work.

1.1 Motivations for electric propulsion and electrospray

For the purposes of traveling to and within space, a propulsion system must be chosen based on its ability to optimally accomplish mission requirements. There are two categories under which one might separate propulsions systems. The first of these two types are those propulsion systems which use propellant as their power source such as chemical rockets. Chemical rockets combust propellants to provide the propelling force and energy by moving the combustion byproduct out of the vehicle. The second of these two types are those propulsion systems which use a power source disjoint from the propellant to propel it out of the vehicle such as electric propulsion vehicles. Electric propulsion systems use energy provided from batteries, solar cells, etc. to accelerate and ionize a propellant gas used to provide a propelling force. These two propulsion types are compared here by deriving basic analytical properties of rocket systems and using them to analyze systems of each kind.

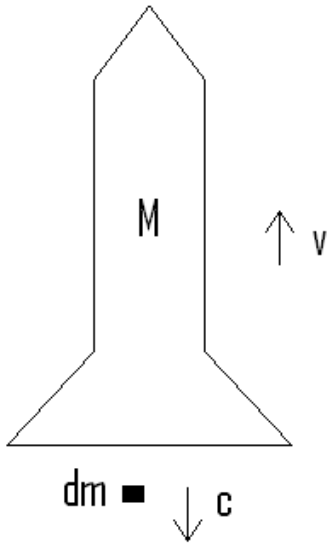

Figure 1-1: Illustration of rocket system.

1.1.1 Analytical Figures of Merit

When no external forces act on a moving rocket, ignoring gravity, momentum is conserved. Thus the total momentum Mv is equal to the momentum when an infinitesimal amount of propellant dm is expelled with velocity c from the vehicle. This is expressed by the following

equation:

$$Mv = (M - dm)(v + dv) + dm(v - c). \tag{1.1}$$

Recognizing that a differential amount of fuel mass expelled is equal to a differential loss in rocket mass gives:

$$dm = -dM. \tag{1.2}$$

Substituting this relation into Eq. (1.1) and ignoring second order terms, this equation simplifies to:

$$Mdv \approx -cdM. \tag{1.3}$$

Eq. (1.3) integrates to give the Tsiolkovsky rocket equation:

$$M = M_0 e^{\frac{-\triangle v}{c}}. \tag{1.4}$$

This implies the following for thrust F which can be found recognizing that momentum is conserved which implies:

$$\frac{d(Mv)}{dt} = M\frac{dv}{dt} + v\frac{dM}{dt} = -\dot{m}(v - c). \tag{1.5}$$

By Eq. (1.2), Eq. (1.5) becomes:

$$F = M\frac{dv}{dt} = \dot{m}c. \tag{1.6}$$

Power P is the rate of increase of the kinetic energy of the propellant in the jet relative to the vehicle which implies that:

$$P = 1/2\dot{m}c^2. \tag{1.7}$$

A figure of merit by which propulsion systems are compared is specific impulse I_{sp}. Specific impulse is impulse per unit weight of propellant:

$$I_{sp} = \frac{\int_0^t F\,dt}{m_{prop}g} = \frac{\int_0^t \dot{m}c\,dt}{m_{prop}g} = \frac{m_{prop}c}{m_{prop}g} = \frac{c}{g}. \tag{1.8}$$

The higher specific impulse an engine has, the less propellant is needed to gain an amount of momentum. Specific impulse is a measure of propellant efficiency. By substituting Eq. (1.8) into Eq. (1.4), it can be seen that for higher specific impulse, a given velocity increase can be obtained for less propellant mass:

$$M_{propellant} = M_0 - M_{final} = M_0(1 - e^{\frac{-\triangle v}{I_{sp}}}). \tag{1.9}$$

Eq. (1.6), Eq. (1.7), and Eq. (1.8) together imply that thrust

$$F = \dot{m}c = \frac{\dot{m}c^2/2}{c/2} = \frac{2P}{gI_{sp}} \tag{1.10}$$

will decrease as I_{sp} increases for a constant power system. Thus, systems with low I_{sp} systems are able to obtain higher thrusts for the same power input while high I_{sp} systems require more power to obtain higher thrusters.

1.1.2 Chemical Rockets

Practically it would seem that using propellant as both your source of power and your momentum transfer is efficient. These kinds of propulsion systems are limited by the amount of energy that can be extracted from their chemical reactions, though. Chemical rockets are thermally limited approximately by

$$E = 1/2mc^2 \leq 5/2kT \tag{1.11}$$

for ideal monotonic gasses. This implies:

$$I_{sp} = c/g \leq \sqrt{\frac{5kT}{mg^2}}. \tag{1.12}$$

Temperature T is limited by the chamber materials temperature limitations and molecular mass m can only go as low as hydrogen. Thus, specific impulse of chemical rockets are limited to less than 500 seconds for an ideal case of hydrogen and oxygen gas with a temperature of 3500 - 4000 Kelvin. Chemical rockets, however, can produce substantial thrust. Eq. (1.10)

shows that for a fixed power, the limited I_{sp} will actually increase thrust produced. Thrust can be increased by increasing thruster power. Thus, if it is necessary to overcome large forces, one needs only to expel more reactive propellant mass per second. For overcoming earth's dense atmosphere, chemical propulsion has no competitors.

1.1.3 Electric Propulsion

Electric propulsion uses electric energy to expel propellant from a vehicle. The energy limitations of these kinds of propulsion systems are determined by the power supply of choice. These systems typically have high power to mass ratios and thus have high specific impulses. High specific impulses are desirable in situations where propellant mass is limited and large ΔVs are required. Because it is so expensive to put payloads into space, efficient use of propellant mass is desirable.

Due to the thrust mechanism of these systems, which usually involve expelling single ions, electric propulsion systems typically do not produce large amounts of thrust. Since these kinds of systems produce high I_{sp}s, it can be seen by Eq. (1.10) that they require high power to produce substantial thrusts. These systems typically thrust for longer periods of time to obtain the same velocity changes as chemical rockets.

Electric propulsion systems can be classified as electrothermal, electrostatic, or electromagnetic systems.

Electrothermal propulsion consists of energizing propellant with resistive heating. Resistojets and Arcjets are two examples of such electrothermal systems. These propulsion systems are illustrated in Fig. 1-2. Resistojets use a resistive conductor to heat propellant which is then expanded through a nozzle. Specific impulse of this process increases with temperature as $\sqrt{T}$ typically reaching $\approx$ 300 sec for a temperature of 2000 K.[21] Arcjets heat propellant with an electric arc. The arc heats and constricts the flow past it producing specific impulses of 500-800 s with hydrazine propellant and 800-1000 s with hydrogen or ammonia propellants.[21],[20]

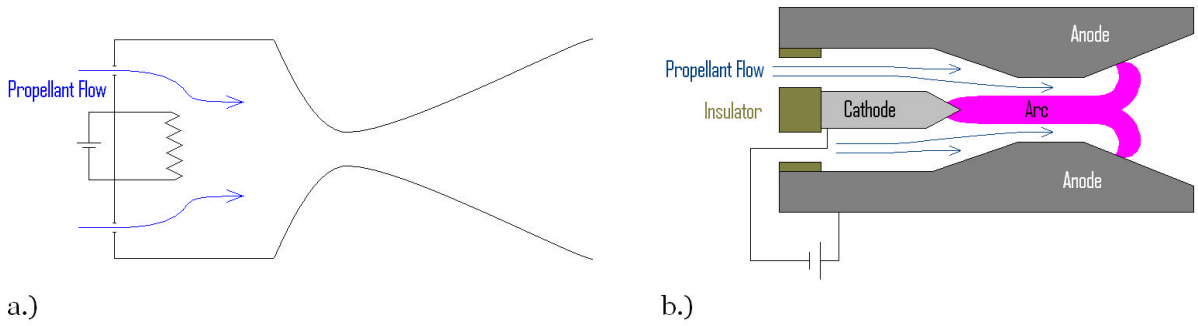

Figure 1-2: Illustration of a.) resistojet and b.) arcjet electrothermal propulsion systems.

Examples of electrostatic thrusters include the ion thruster and electrospray propulsion. Ion thrusters use electrostatic fields to accelerate ionized propellant gas. The ionized gas is produced and magnetically confined in the ionization chamber. Ion engines produce specific impulses of ≈ 2500-7500 s and have demonstrated 20,000 hours of operation.[21],[20] Electrospray propulsion uses a large electric field to extract ions and charged droplets from a conducting liquid surface. Electrospray that uses liquid metal propellants is call Field-Effect Electrostatic Propulsion (FEEP). FEEP thrusters extract ions from the propellant. Electrospray systems that use nonmetallic liquids and expel charged droplets are called colloid thrusters. Electrospray thrusters can extract either ions, submicron droplets, or a mixture of both. These electrospray mechanisms produce hundreds to thousands of seconds of specific impulse for about 1–10 kV applied voltage.[21] Figure 1-3 illustrates these propulsion systems.

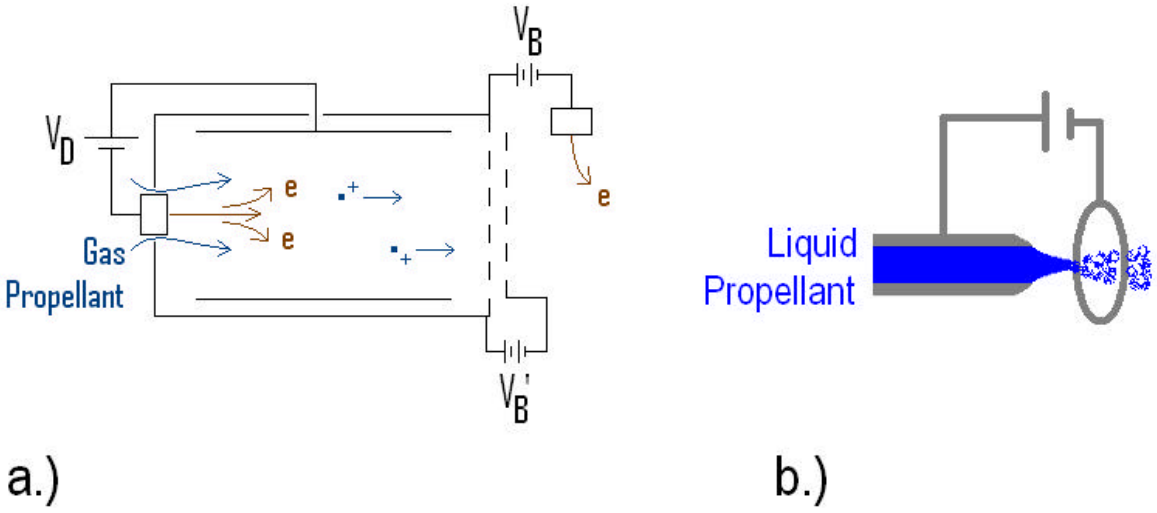

Figure 1-3: Illustration of an a.) ion engine and b.) electrospray as examples of electrostatic propulsion systems.

On the border between electrostatic and electromagnetic thrusters there is the Hall effect thruster or Hall thruster. Hall thrusters have an external cathode which produces both beam electrons as well as electrons that flow opposite to the propellant gas. The counterflowing electrons ionize the propellant gas which is accelerated out of the thruster by an electrostatic field formed by the external cathode and an internal anode. A radial magnetic field is used to confine electrons in the ionization region of the thruster without confining ions. Although particles are accelerated electrostatically, the thrust created by the Hall thruster is applied to the magnetic coils through their interaction with the electron Hall current making the thruster somewhat electromagnetic. Figure 1-4 illustrates this mechanism of operation. A typical Hall thruster produces $\approx$ 1500 s I_{sp} for an applied 300 V and 3000 s for 1000 V.[21],[20]

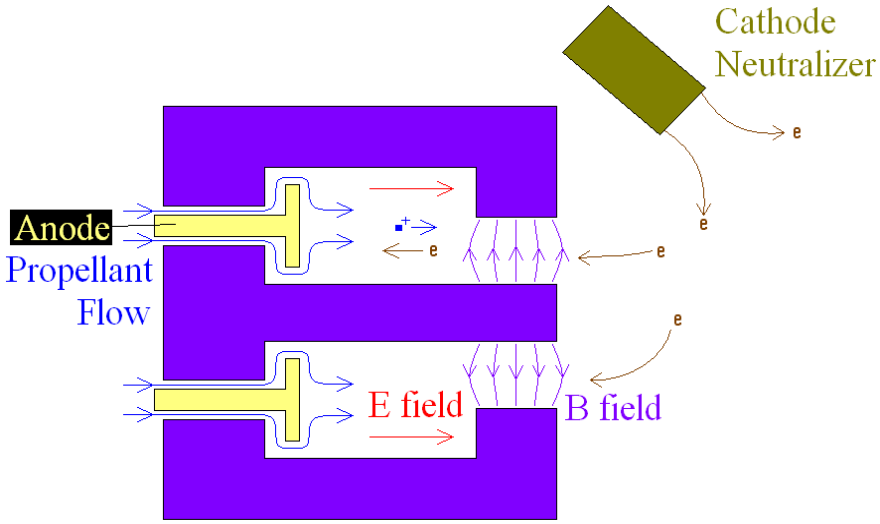

Figure 1-4: Illustration of Hall thruster.

Magnetoplasmadynamic (MPD) thrusters and pulsed plasma thrusters (PPT) are examples of electromagnetic thrusters. See Fig. 1-5 for illustrations of these thrusters. The MPD passes a radial current through the open section which collides with and ionizes the propellant gas. The current also completes the current loop thus inducing an azimuthal magnetic field. This magnetic field produces a Lorenz $J \times B$ force on the ionized gas producing thrust. MPD thrusters produce high thrusts due to their megawatt power levels and have specific impulses around 2000 s.[21] PPTs operate in a similar way as MPD thruster but use solid propellant instead of gaseous propellant. A solid block of inert propellant (usually

Teflon®) is ionized with an arc from a capacitor discharge. The ionized particles flow in the electric field established by the anode and cathode. The arc of current induces a magnetic field which produces a Lorenz $J \times B$ force on the ionized particles causing thrust. Thruster operation is pulsed due to the charging and discharging of the capacitor. The PPT operates at high power with specific impulses of 1000 – 1500 s.[21]

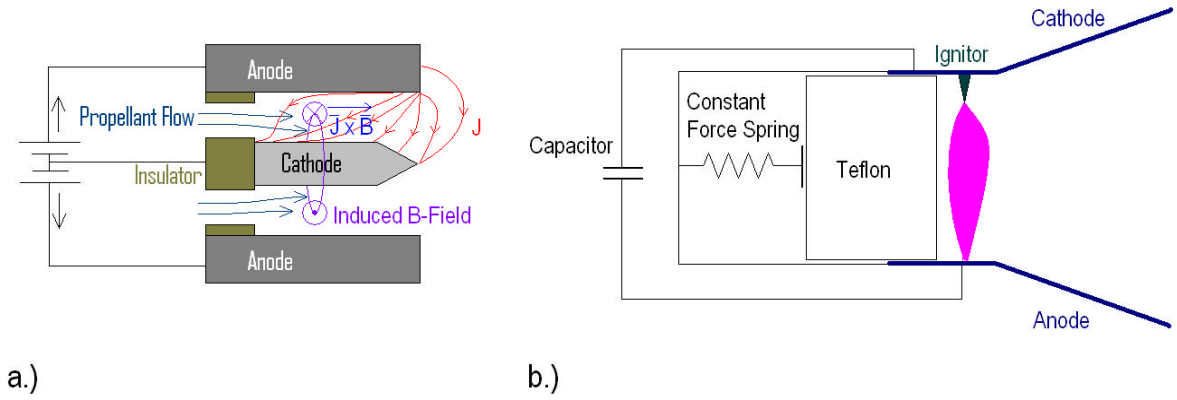

Figure 1-5: Illustration of a a.) magnetoplasmadynamic (MPD) thruster and a b.) pulsed plasma thruster (PPT) as examples of electrostatic propulsion systems.

1.2 Electrospray physics

1.2.1 Liquid surface instability and starting voltage

When a conducting liquid surface is exposed to a large enough electric field it can become unstable. The forces acting on the liquid free surface are electric traction countered by the liquid surface tension. In equilibrium the balance can be expressed as:

$$\frac{1}{2}\varepsilon_0 {E_n}^2 = \frac{2\sigma_{LV}}{R_c}. \tag{1.13}$$

If the level liquid surface has a perturbation the electric traction will intensify at the higher liquid portion and weaken at the lower liquid portion as can be seen in Fig. (1-6). A linearized stability analysis shows that instability will occur for electric field values larger

than:

$$E_{crit} = \sqrt{\frac{2\pi\sigma_{LV}}{\lambda\varepsilon_0}}, \tag{1.14}$$

where λ is the perturbation wavelength and is equal to $2D$ for a meniscus of liquid held at the end of an open capillary of diameter D. Thus, an analysis of a conducting meniscus of liquid held at the end of a capillary tube a distance d from an electrode will produce a Taylor cone at a minimum applied voltage of:

$$V_{start} = \sqrt{\frac{\sigma_{LV} D}{2\varepsilon_0}} ln\left(\frac{8d}{D}\right). \tag{1.15}$$

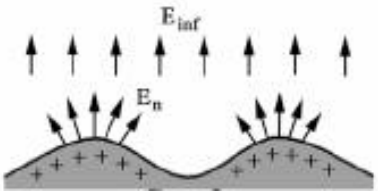

Figure 1-6: Illustration of conducting liquid instability due to an applied electric field taken from Ref. [19]

1.2.2 The Taylor cone

When the meniscus of a conducting liquid is immersed in a sufficiently strong electric field, the liquid forms a conical structure known as a Taylor cone caused by the balance between electrostatic traction and the surface tension forces in the liquid. This phenomena was first analytically described by Taylor who suggested that the cone will have a constant cone angle.[30]

To calculate the Taylor cone angle, consider an equipotential cone such as the one shown in Fig. 1-7. Making the origin of the coordinate system at the top can center of the cone, we obtain cone curvature as the following:

$$\frac{1}{R_c} = \frac{1}{R} cos\alpha = \frac{cos\alpha}{r sin\alpha} = \frac{cot\alpha}{r}, \tag{1.16}$$

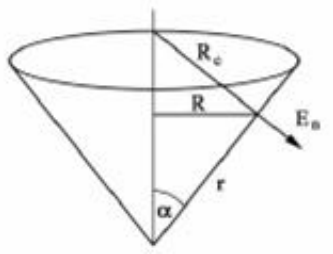

Figure 1-7: Illustration of equipotential cone taken from Ref. [19]

where R_c is the distance from the origin to a point on the cone surface, R is the perpendicular distance from the cone center line to a point on the cone surface, α is the cone angle, and r is the distance from a point on the cone surface to the cone apex. To have equilibrium, the sum of the forces acting on the cone surface must be zero. This force balance implies that electric pressure is equal to the liquid surface tension:

$$\frac{1}{2}\varepsilon_0 {E_n}^2 = \frac{\sigma_{LV} cot\alpha}{r}, \tag{1.17}$$

where ε_0 is the permittivity of free space, E_n in the normal electric field and σ_{LV} is the surface tension of the liquid. Equation (1.17) can be solved for the electric field as:

$$E_n = \sqrt{\frac{2\sigma_{LV} cot\alpha}{\varepsilon_0}} r^{-1/2}. \tag{1.18}$$

By the definition of electric potential ϕ for this electroquasistatic system:

$$E_n = -\bigtriangledown_n \phi. \tag{1.19}$$

By Gauss's law:

$$\bigtriangledown_n E_n = -{\bigtriangledown_n}^2 \phi = \frac{\rho_f}{\varepsilon_0}. \tag{1.20}$$

Assuming no free charges on the liquid surface $\rho_f = 0$ makes Eq. (1.20) a Laplacian equation which can be solved by a product of Legendre functions in spherical coordinates of the form:

$$\phi = AP_\nu \left(cos\theta\right) r^\nu \tag{1.21}$$

and

$$\phi = AQ_\nu\left(cos\theta\right)r^\nu, \tag{1.22}$$

where P_ν are the Legendre functions of the first kind and Q_ν are the Legendre functions of the second kind. Legendre functions of the first kind P_ν have a singularity at $\theta = 180°$ while the Legendre functions of the second kind Q_ν have a singularity at $\theta = 0°$. Since it is desired to solve for the area with $\theta > 0°$ solutions of Legendre functions of the first kind P_ν are thrown out. Substituting Eq. (1.22) into Eq. (1.19) gives:

$$E_n = -\bigtriangledown_n\phi = -\frac{1}{r}\frac{\partial\phi}{\partial r} = A\frac{dQ_\nu}{d\left(cos\theta\right)}sin\theta\frac{1}{r^{1-\nu}}. \tag{1.23}$$

By Eq. (1.18), $E_n \propto r^{-1/2}$ implying that $\nu = 1/2$ and by Eq. (1.22):

$$\phi = Ar^{1/2}Q_{1/2}\left(cos\theta\right). \tag{1.24}$$

Note that this equation could also be written in terms of Legendre functions of the first kind with the substitution $Q_{1/2}\left(cos\theta\right) = P_{1/2}\left[cos\left(180° - \theta\right)\right]$. Arbitrarily imposing the potential of the cone surface to be zero, Eq. (1.24) can be solved to find Taylor's relation that the Taylor cone will have a constant angle $\theta = \alpha = 49.290°$.

1.2.3 Surface electrostatics

After an infinite amount of time in a static system the electric field in a conductor will go to zero. By Gauss's law, the surface free charge can be calculated to be:

$$\sigma_f = \varepsilon_0 E_n, \tag{1.25}$$

where σ_f is the surface free charge on the liquid, ε_0 is the permittivity of free space, and E_n in the normal electric field. See Fig. (1-8) for an illustration of the Gaussian surface of integration.

For a dielectric surface with dielectric constant ε in a static electric field, Gauss's law for

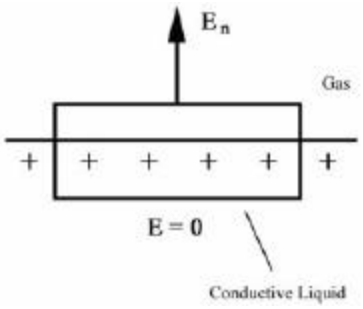

Figure 1-8: Illustration of conducting surface in electrostatic equilibrium taken from Ref. [19]

electricity implies

$$\varepsilon_0 E_{n,g} - \varepsilon_0 \varepsilon E_{n,l} = \sigma_f. \tag{1.26}$$

See Fig. (1-9) for an illustration of the Gaussian surface.

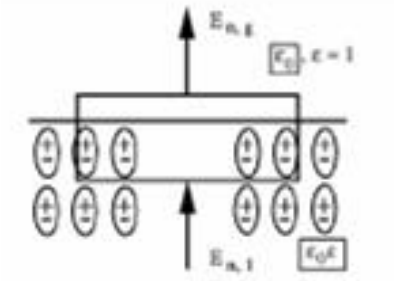

Figure 1-9: Illustration of dieletric surface in electrostatic equilibrium taken from Ref. [19]

Ohm's law says:

$$\frac{d\sigma_f}{dt} = K E_{n,l}, \tag{1.27}$$

where K is the conductivity of the liquid. Substituting Eq. (1.26) allowing surface free charge due to transient times into Eq. (1.27), the following differential equation is obtained:

$$\frac{d\sigma_f}{dt} + \frac{K}{\varepsilon_0 \varepsilon}\sigma_f = \frac{K}{\varepsilon} E_{n,g}. \tag{1.28}$$

Assuming a constant applied field $E_{n,g}$, this equation can be solved as:

$$\sigma_f = \frac{E_{n,g}}{\varepsilon_0}\left(1 - e^{-\frac{t}{\tau}}\right), \tag{1.29}$$

where $\tau = \frac{\varepsilon_0 \varepsilon}{K}$ is the relaxation time of the liquid in response to an externally applied electric field.

1.2.4 Cone jet and current emission

At large enough potentials to produce a Taylor cone, one also has a structure known as a cone jet in which a thin jet of charged particles and droplets is emitted from the cone tip. Theoretical modeling, non-dimensional analysis, and experimentation presented in reference [8] provides explanation of flow and current emitted from a cone jet. Those results are presented here.

Since a stable cone jet mode will have fluid flowing to the Taylor cone apex at a rate Q, there will be a fluid velocity increasing as $1/r^2$. At some point near the Taylor cone apex the "residence time" or the time it takes flowing liquid moving towards the cone apex to be ejected will be less than the charge relaxation time computed in subsection (1.2.3). This residence time is of the order r^3/Q where Q is the volumetric flow rate of the fluid. The residence time thus becomes the same as the relaxation time at the characteristic apex distance:

$$r^* = \left(\frac{\varepsilon \varepsilon_0 Q}{K}\right)^{1/3}. \tag{1.30}$$

So for distances $r < r^*$, more charge will not be conducted to the cone jet and the collected charge at r^* will be convected by the flow. Convected current I is proportional to the ring of charge at r^* which is equal to $(2\pi r^* \sigma_f)$ times the velocity at r^* which goes as Q/r^{*2}. Thus, $I \propto \frac{Q}{r^*}\sigma_f$ and from Eq. (1.25) $\sigma_f \propto \varepsilon_0 E_n$ implying $I \propto \frac{Q}{r^*}\varepsilon_0 E_n$. From Eq. (1.18) $E_n \propto \sqrt{\frac{\sigma_{LV}}{\varepsilon_0 r^*}}$ which implies:

$$I \propto Q\sqrt{\frac{\sigma_{LV}\varepsilon_0}{r^{*3}}}. \tag{1.31}$$

Substituting Eq. (1.30) into Eq. (1.31) the following relation if found for current emission from the cone jet based on flow rate and fluid properties:

$$I \propto \sqrt{\frac{\sigma_{LV} K Q}{\varepsilon}}. \tag{1.32}$$

From experimental work in reference [8] it was shown that the factor making the proportionality in relation (1.32) can only vary with ε making:

$$I = \frac{f(\varepsilon)}{\sqrt{\varepsilon}}\sqrt{\sigma_{LV} K Q}, \tag{1.33}$$

1.2.5 Ion and droplet spray regimes

For large enough electric fields, which implies small enough flow rates, ions can be extracted from a Taylor cone surface instead of the droplet emission described in the previous subsections. The conditions for ion emission from charged droplets are described in reference [12]. Since ions are much lighter than droplets, there is a big difference in particle speeds making mixed ion/droplet sprays inefficient. It is desirable to produce sprays consisting completely of ions or completely of droplets. Droplets produce larger thrusts due to their large masses but typically have inefficiency due to polydispersion. Ions will have much faster exit speeds, will produce higher specific impulses, and are typically monodisperse. Reduction of flow should in princliple lead to the pure ion regime in any fluid, but so far only Ionic Liquids have been seen to emit pure ions.[27] In other liquids, the cone-jet regime breaks down to an intermittent operation before the liquid drops disappear.

1.2.6 Polarity alternation

A downside to thruster operation is the potential for electrochemistry in one mode or the other to cause degradation on emitter surfaces. As charged particles are emitted from the electrospray propellants, particles of the opposite polarity neutralize on the emitter surface. These neutralizing "counter-ions" can react with the emitter causing corrosion, they can merely deposit on the emitter, they can form bubbles, or they can diffuse into the spray.[19]. Fortunately, experiment has shown that these processes will not occur until a sufficient amount of charge has built up on the emitter devices.[17] Thus, such reactions can be avoided by alternating voltage before reactions can occur. This switching between positive and negative particle emission is referred to as bipolar operation.

Beam neutralization is a concern for most electric propulsion devices including electrospray. Like the ion thruster or Hall thruster, electrospray thrusters can operate by extracting positive particles from a propellant and using an external cathode to neutralize the beam. This systems introduces complexity. An advantage of bipolar operation is its use for beam neutralization without the need for an external cathode.

1.3 Relevant previous electrospray thruster work

The theoretical basis for the formation of a Taylor cone was first given by G. I. Taylor in 1964 although the phenomenon was observed as early as 1600.[30],[10]

Electrospray propulsion was first studied for the purposes of propulsion in the 1960s.[28] The bulk of this research consisted of studies using electrospray. Research into negative particle emission was begun by the US Air Force and TRW.[32],[13] The first bipolar thruster was built by the Air Force Aero Propulsion Laboratory at the Wright Patterson Air Force Base in Ohio and TRW.[14] The use of bipolar operation (half the emitters operating in the positive mode and the other half operating in the negative mode) allowed a electrospray thruster to be used without the need of an external neutralizer.

Electrochemical interactions between propellant and emitters causing capillary clogging bubbles and erosion prompted study of these electrochemical interactions.[14],[26],[29],[33] An idea of AC stitching of emitter polarity to prevent or undo electrochemical processes and produce quasineutral plasmas was explored by TRW.[6] Work was also done between 1975 and 1978 to understand these degradation problems.[24]

By the end of the 70s, most electrospray thruster work ended in the USA and Europe. Interest and work in the field did not resume until the late 90s as the emergence of microspacecraft caused a renewed need for electrospray.[22]

Around this time of renewed interests, the idea of microfabrication of electrospray thrusters came about.[25],[23] The idea of externally wetted tungsten and silicon emitters was studied

at MIT due to the emergence of ionic liquid propellants with near zero pressure. Electrospray propulsion devices using ionic liquids with externally wetted architectures have shown emission in the pure ion regime and μA of current with voltages less than 3kV.[5],[27],[18],[16] Another obvious advantage of externally wetted thrusters is that they cannot be clogged like capillary emitters.

The interactions of this external fluid flow with electrospray performance are being studied in greater detail at MIT. These studies include understanding how propellant will spread over a dry silicon thruster surface. Models of the spread of small, non-reactive liquid droplets on perfectly smooth solid substrates have been presented that match well with experimental data.[11] However, the behavior of fluid spread over surfaces roughened for increased wettability is no so well understood.

1.4 Research purpose and objectives statement

This research is intended to find a black silicon treatment which gives complete wetting of a silicon thruster surface and develop a model of the spread of a propellant drop over a dry black silicon surface which agrees well with experimental data.

Silicon wettability was analyzed by producing samples with various black silicon treatments and performing five analyses: atomic force microscope (AFM) measurements to determine average surface roughness, contact angle measurements with the EMI-BF_4 and EMI-IM, scanning electron microscope (SEM) measurements to determine surface geometry, spreading rate experiments to analyze dynamic wetting properties, and thruster tests to verify thruster current output. Based on these wettability measurements, an optimal wetting treatment was determined.

A propellant spread model was developed based on accepted theory for fluid spread over a smooth substrate. This theory was extended to include the substrate roughness by analytically describing the spreading behavior observed in experiment.

Chapter 2

Black Silicon Treatments

Black silicon is silicon whose surface has been etched to have nanometer to micrometer structured features. Black silicon is named for its characteristic opaque color. For some, black silicon is a annoying byproduct of etching methods. For others, however, the ability of black silicon to produce hydrophobic, hydrophilic, and light absorbing surfaces make it an attractive area of study.

Besides making thruster surfaces wettable, black silicon has various other applications. Black silicon can alternatively be used to make hydrophobic surfaces. Hydrophobic surfaces have less contact area with liquids reducing erosion, friction, and contamination which is beneficial for many applications.[2] Studies have explored the application of black silicon to solar cells.[1] The opaque appearance of black silicon makes its surface less reflective than untreated silicon surfaces. This ability of black silicon to absorb light, makes it more efficient at converting light to energy than standard silicon solar cells with an anti-reflective coating. Application of black silicon to photodiodes has been shown to extend its photoresponse to visible wavelengths.[3]

2.1 Fabrication Methods

Black silicon can be formed by at least three possible ways: laser etching, gold Etching, or plasma etching.

The Mazur Group at Harvard University has formed black silicon by irradiating a silicon surface with femtosecond laser pulses in the presence of a sulfur containing gas. This process forms closely spaced microscopic spikes.[3]

Koynov and his colleagues at the Technical University of Munich form black silicon by first depositing grains of gold only nanometers large onto a flat silicon surface. Next, they etch the exposed silicon with a solution of hydrogen peroxide and hydrofluoric acid. The gold nanoparticles catalyze the etch. The nanoparticles are then removed with a solution of iodine and potassium iodide. The areas which were covered by the gold form 50-to-100-nanometer-high silicon hills.[1]

Black silicon is more commonly formed by dry plasma etching called a Reactive Ion Etch (RIE). In this process, an ionized reactive gas species, Chlorine for example, causes a chemical etch which is anisotropically enhanced by ion bombardment due to high kinetic energies. When the silicon surface begins to etch, silicon oxide particles cover the silicon effectively masking the silicon and causing the surfaces to be etched in rough patterns. This process which forms black silicon is called micromasking. The process used in this research is shown in Appendix A.

2.1.1 Initial silicon surface

These black silicon treatments are meant to be used as a final step in the fabrication of silicon thruster arrays. Based on the fabrication methods that have been used thus far in the fabrication of MIT electrospray thruster arrays, the samples were etched with a SF_6/C_4F_8 Deep Reactive Ion Etch (DRIE) prior to the black silicon treatments.

The DRIE was done with a ST Systems Multiplex Inductively Coupled Plasma (ICP) tool

which produces anisotropic etching of the silicon. The tool uses two independent 13.56MHz Radio Frequency (RF) power supplies - a 1000W supply for a single-turn coil around the etch chamber and a 300W supply connected to the wafer electrode to vary the RF bias potential of the wafer with respect to the plasma. The coil power is inductively coupled to the plasma to produce high plasma densities. The tool uses the Bosch process of alternating an SF_6 etch cycle and a C_4F_8 sidewall passivation cycle. The passivating film created by the C_4F_8 is preferentially removed from the bottom of trenches with ion bombardment from the SF_6 plasma causing an isotropic etch.

2.1.2 Black silicon samples made

Black silicon treatments made in this research were done with a PlasmaQuest Electron Cyclotron Resonance (ECR) plasma etcher. ECR achieves higher density plasmas than ICP with the use of a confining magnetic field. Treatments were done with varied Cl_2/He working gas flow rates, bias power levels, source power levels, chamber pressures, and etch times. Wetting results presented in chapter 3 were taken simultaneously with the fabrication of the black silicon treatments to provide an elimination process for optimal sample selection. Each measurement or experiment provided data that allowed treatments that were unlikely candidates for favorable externally wetted thruster performance to be discarded. Silicon surfaces with initial etches described in section 2.1.1 had varied final black silicon treatments described in Table (2.1). Treatments were numbered 1, 2, 3, 4, 1′, 2′, 3′, 4′, 5′, 6′, 7′, 8′, 9′, 10′, 11′, 12′, 1″, 2″, 3″, and 4″.

Table 2.1: Etch parameters for silicon samples made to test wettability

Etch Times	Low Values	High He	High Press	High Bias	High Power	**Key of Parameters:**
						$6'$ –untreated silicon
5 min	1			4	2	Chlorine flowrate for all samples: 150 sccm
5 min				3		
7.5 min	$1\ '$		$5'$	$4'$	$2'$	
7.5 min				$3'$		
9 min		$9'$	$8'$	$7'$		
9 min			$10'$			
9 min		$12'$				
9 min		$11'$				
10 min		$3''$	$2''$	$1''$		
10 min			$4''$			

	High Value	Low Value
Helium –	60 sccm	30 sccm
Pressure –	50 mTorr	25 mTorr
Bias –	40 W	20 W
Source –	400 W	200 W

Note: Cells contain sample #'s

Note: Unless indicated otherwise, all parameters for a given sample are at the lower value.

Chapter 3

Experimental Methods

This chapter describes the methods used to measure the wettability of the the various black silicon treatments and determine the treatments which would produce the most favorable performance. This chapter also outlines the spreading rate experiments that are later compared with theory from chapter 4 in the results and sources of error in this experiment.

3.1 AFM Measurements

An Autoprobe CP Atomic Force Microscope was used for AFM measurements. The average surface roughness values of the black silicon surfaces were measured with an atomic force microscope (AFM) and are plotted in Fig. 3-2. The average surface roughness R_a is defined as the average deviation between the roughness profile and its mean line, or the integral of the absolute value of the roughness profile height measured from surface height average, divided by the area:

$$R_a = \frac{1}{L_2}\frac{1}{L_1}\int_0^{L_2}\int_0^{L_1} |r(x,y)|\, dxdy, \tag{3.1}$$

where r(x,y) is the height of the surface at a position with coordinates (x,y). See Fig. 3-2 for an illustration.

According to Table 2.1, rougher samples were produced by the 9 minute treatments as

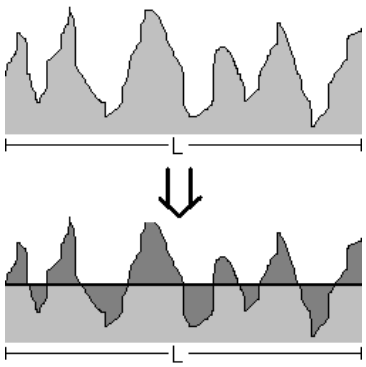

Figure 3-1: Illustration of average sample surface roughness.

opposed to longer treatments. This trend implies that the treatment roughness reaches a maximum with respect to etch time. The general assumption is that the rougher the sample surface is, the greater wettability it will have (assuming roughness peaks are not too large). Thus, the rougher surfaces were considered better candidates for wettability.

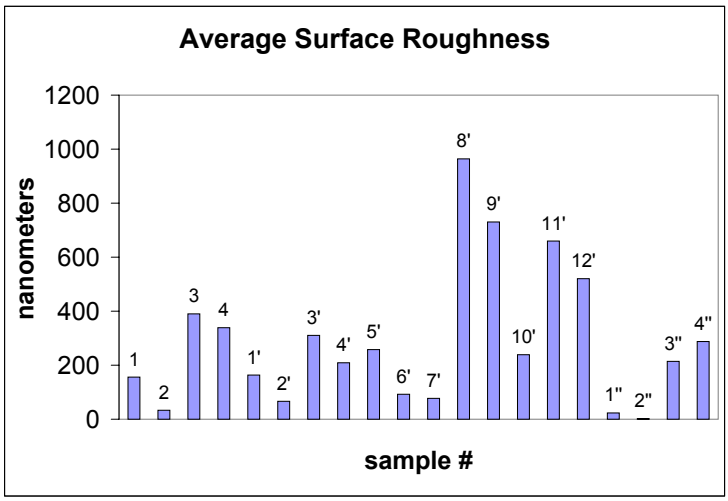

Figure 3-2: Average of the magnitude of surface height deviations from the average surface height found from AFM measurements

3.2 Goniometer Measurements

A Ramé-Hart contact angle goniometer model 100 was used to find static contact angle measurements. Contact angle measurements of both EMI-BF_4 and EMI-IM on the samples were made. The contact angle of three to six drops of sizes ranging from a few hundred nL to a few μL of each propellant per sample was measured no more than a minute after

the drop was placed on the sample surface. The contact angles measured were not always at their equilibrium value. The near-zero contact angles are less accurate than the large contact angles measured because these samples did not reach an equilibrium value within a minute and continued to spread.

Contact angle measurements are displayed in Fig. 3-3. By definition, a surface is considered wettable if it has a contact angle less than 90°. Thus, the lower a contact angle a surface has, the more wettable it is. It is somewhat counterintuitive that samples 1′, 5′, 10′, 2″, and 3″ with small roughness values seen in Fig. 3-2 had fairly low measured contact angles seen in Fig. 3-3.

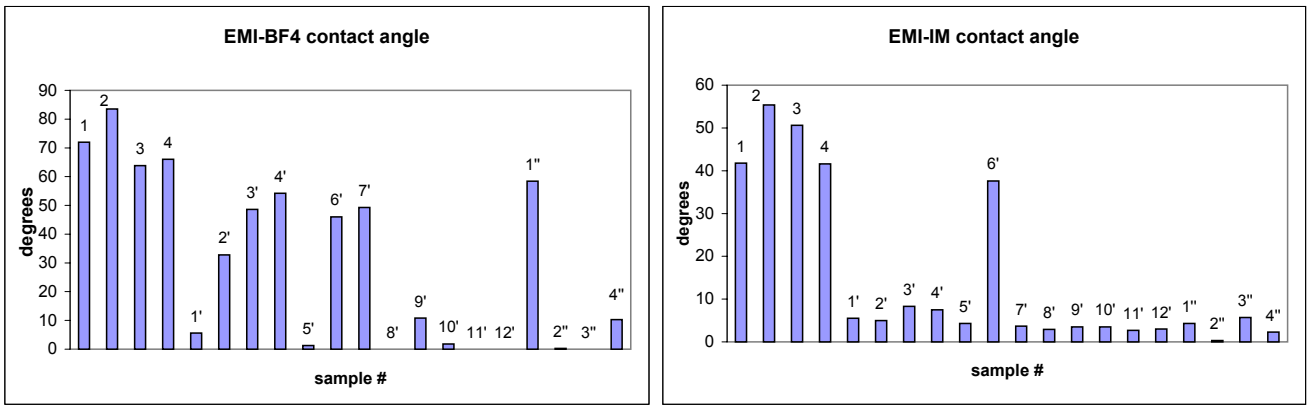

Figure 3-3: Average contact angle measurements of a) EMI-BF_4 and b) EMI-IM on silicon samples with various black silicon samples.

3.3 SEM Measurements

Eight of the samples were selected for propellant spreading rate tests and to take Scanning Electron Microscope (SEM) measurements. These were samples 2, 2″, 5′, 8′, 9′, 10′, 11′, and 12′. Sample 2 had one of the lowest roughness and the highest contact angle and thus was picked for comparison purposes. The remaining samples were chosen because they had lower contact angles and thus were considered "good" samples. Figure 3-4 shows the surfaces of samples 2, 8′, and 10′, all at the same magnification.

It is interesting to note that, sample 2 had the lowest measured roughness. Figure 3-4 shows that sample 2 actually has close packed peaks. The closeness of the large peaks in sample

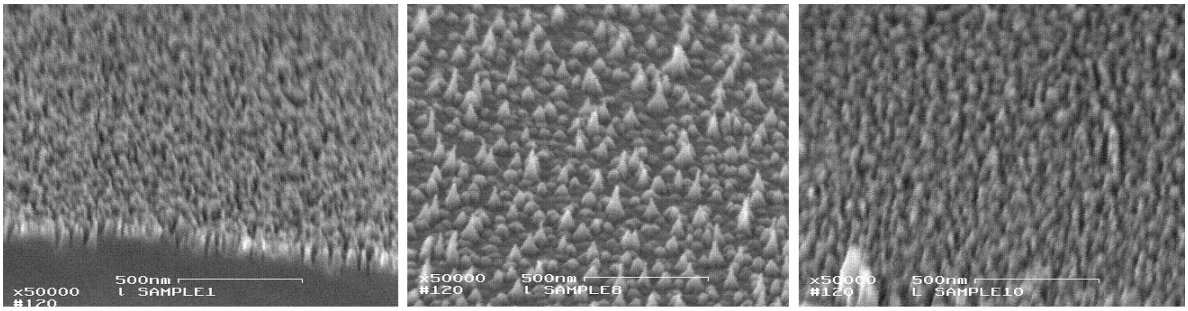

a.) b.) c.)

Figure 3-4: SEM images taken at a 30° angle with 500 nm resolution of samples a) 2, b) 8′, and c) 10′.

2 may have been outside the AFM depth resolution thus causing the surface to appear smooth. A close look at sample 8′ shows tall peaks with smooth gaps between them. These tall peaks would explain why sample 8′ had the largest value of average surface roughness. The smooth spaces between the large peaks of sample 8′ might suggest that its surface could have wetting problems and perhaps slow spreading rates. Sample 10′ had a fairly average surface roughness but Fig. 3-4 shows peaks which are closely spaced.

Figure 3-5 shows samples 2″, 5′, and 9′ which had smoother surfaces than those samples shown in Fig. 3-4 yet, these samples have small contact angles, an effect not understood.

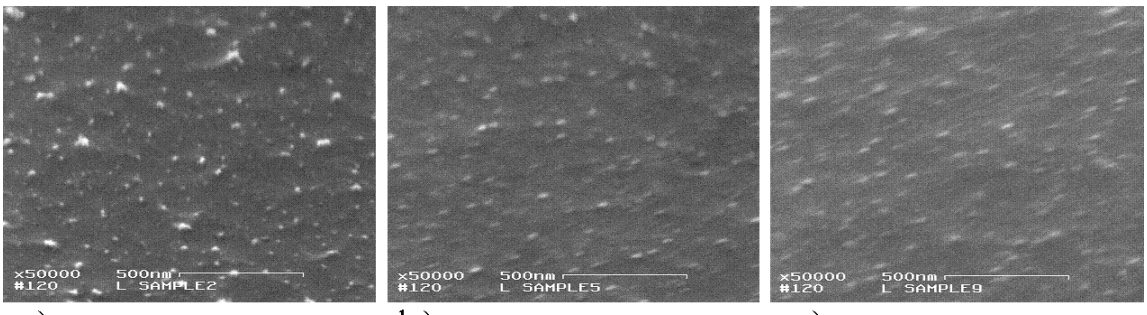

a.) b.) c.)

Figure 3-5: SEM images taken at a 30° angle with 500 nm resolution of samples a) 2″, b) 5′, and c) 9′.

3.4 Spreading Rate Measurements

Spreading rate experiments consisted of video taping the spread of a 1 μL sessile drop on a sample and using Matlab to analyze its increase in area with time. Figure 3-6 illustrates the experiment which consisted of a capillary tube attached to a syringe pump (not seen) and held above the silicon substrate to deposit the propellant. The spread of the drops were observed with a video camera at an approximate angle of 45° to the substrate surface and the images were analyzed frame by frame with Matlab to determine the drop base area as a function of time. Each experiment analyzed drop spreading for about 12.5 minutes. An example of the Matlab code used to analyize the data is shown in Appendix B.

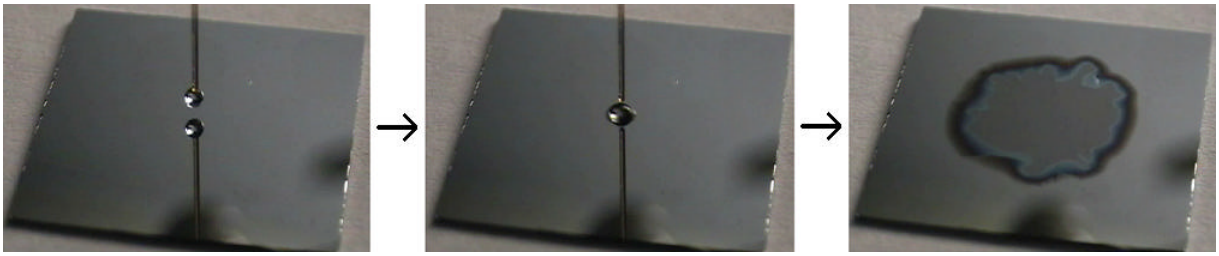

Figure 3-6: The first image in the series shows the 1 μL drop above the substrate suspended at the end of a capillary, the second image shows the drop being placed on the substrate surface, and the third image shows the drop spread after approximately 12.5 minutes.

There are a few sources of error in the experiments. The views of the images were assumed to be two-dimensional top views in the analysis which introduced a source of error. The 1 μL drops of propellant were placed on each substrate by lightly touching the liquid meniscus to the substrate surface because the drops were not massive enough to fall under their own weight. This caused an initial force and drop radius variation that was ignored in the analysis. This method of depositing the drops and the variations in camera angle are predicted to be the major limits in the repeatability of the experiments.

3.5 Thruster Performance

The experimental setup for the thruster array tests consisted of 4 parts diagramed in Fig. 3-7. The first was the 4×4 silicon emitter array (16 emitters) (a). A stainless steel extractor (b)

with 1.8 mm diameter holes was suspended approximately 1.4 mm in front of the emitters. A negative potential of 3 kV was applied between the emitter and the grounded extractor. A tungsten grid (c) was suspended in front of the emitter/extractor assembly and biased to -50 V to suppress secondary electron emission. The final portion of the experimental setup consisted of a stainless steel collector plate (d). A Keithley 6514 electrometer was used to measure the current collected by the collector plate. The entire experimental assembly was kept at room temperature inside a vacuum chamber with a pressure less than 2×10^{-6} Torr. Only samples $2''$, $10'$, and $9'$ were tested on 4×4 thruster arrays because there were a limited number of fabricated thruster arrays available and these treatments were chosen as likely candidates for producing favorable thruster performance.

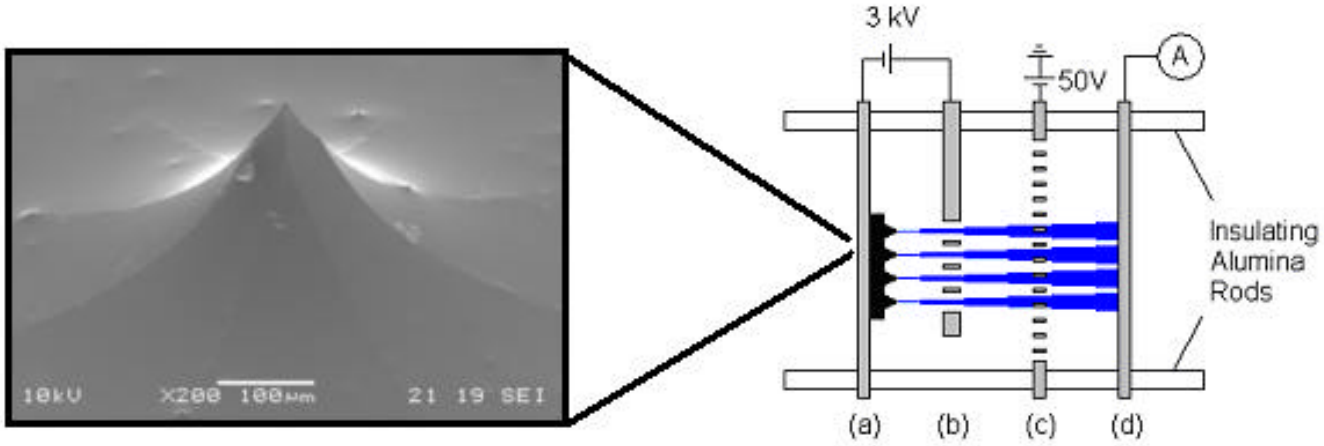

Figure 3-7: Diagram of experimental setup used to test 4×4 silicon thruster arrays with black silicon with close up SEM view of individual thruster. treatment.

Chapter 4

Theoretical Analysis

This chapter describes a theoretical model of the spread of a small, non-reactive propellant drop over a roughened silicon surface. This analysis was based on theory in Reference [11] and additional theory developed to describe experimental observations.

4.1 Spreading Regimes

In our spreading model, fluid spread consisted of three regimes in which different forces dominated the spreading. The first spreading regime is the inertial spreading regime where inertial forces dominate the spreading process. The next is the viscous spreading regime where viscous forces dominate the spreading process. The first two spreading regimes are based completely on theory presented in Reference [11] which describes the spread of a small, non-reactive fluid drop over a perfectly smooth substrate. The third spreading regime was developed to describe a thinner, darker front of spreading liquid that can be seen in the third frame of Fig. (3-6). The third spreading regime is the porous spreading regime where spread consists of porous flow through the rough substrate surface whose pressure driven flow source is a constant contact angle drop with a constant radius less than the entire spread radius.

4.1.1 Inertial spreading

In spreading dominated by inertial forces, the triple line of the drop will quickly reach an equilibrium angle θ_F which is independent of time. The triple line is the line where the liquid, solid, and vapor meet. The drop spread will then be dominated by inertial forces which cause the drop to have a non-spherical shape. Fig. 4-1 illustrates this spreading.

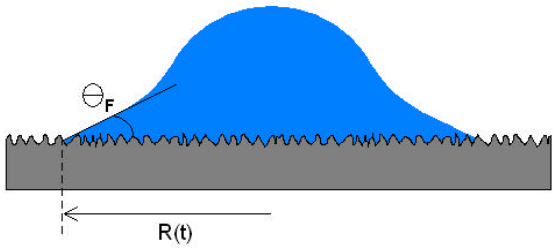

Figure 4-1: Illustration of fluid spread dominated by inertial forces.

For inertial spreading, assume the drop takes a circular base area A with an initial radius R_0. According to Reference [7], a balance of capillary energy and kinetic energy implies

$$U \approx \left[\frac{\sigma_{LV}}{\rho R_0}\right]^{1/2}, \tag{4.1}$$

where U is the triple line velocity (such that $U = \frac{dR}{dt}$, the rate of change of the drop radius R with respect to time t), σ_{LV} is the liquid surface tension, and ρ is the propellant density. Since σ_{LV}, ρ, and R_0 are constants for the given conditions, U is a constant value. The increase of drop area is governed by the following equation

$$A = \pi R^2 = \pi \left(R_0 + Ut\right)^2. \tag{4.2}$$

The substitution of Eq. (4.1) into Eq. (4.2) yields the following equation for area versus time:

$$A_{iner} = \pi \left[R_0 + \left(\frac{\sigma_{LV}}{\rho R_0}\right)^{1/2} t\right]^2. \tag{4.3}$$

Taking the derivative of Eq. (4.3) with respect to time, the following relation is found for inertial spreading:

$$\frac{dA_{iner}}{dt} = 2\pi \left[R_0 + \left(\frac{\sigma_{LV}}{\rho R_0} \right)^{1/2} t \right] \left(\frac{\sigma_{LV}}{\rho R_0} \right)^{1/2}. \tag{4.4}$$

4.1.2 Viscous spreading

In spreading dominated by viscous forces, the drop will retain a spherical cap shape and the main energy dissipation will occur along the triple line. Because the motion of the drop edge is limited, the contact angle will be a function of time. Fig. 4-2 illustrates this spreading.

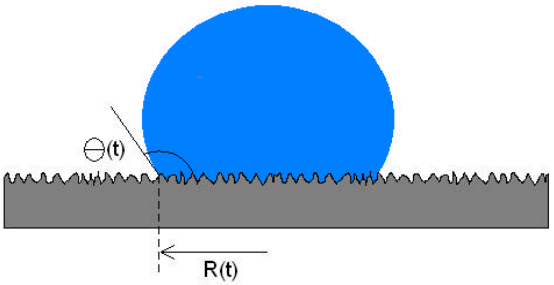

Figure 4-2: Illustration of fluid spread dominated by viscous forces.

For viscous spreading, a balance of viscous energy dissipation with change in surface and interfacial energy at the triple line gives the relation:

$$\frac{3\eta K_1 U^2}{tan\theta} = \sigma_{LV} \left(cos\theta - cos\theta_F \right) U. \tag{4.5}$$

where η is the dynamic viscosity, K_1 is the logarithm of the ratio of macroscopic droplet size to the thickness of the liquid slippage layer (≈ 10), again U is the triple line velocity, θ is the time-dependent contact angle, and θ_F is the final equilibrium contact angle of the drop defined by $cos\theta_F = \left(\sigma_{SV} - \sigma_{SL} \right) / \sigma_{LV}$ where σ_{SV} is the surface energy and σ_{SL} is the interfacial energy.

Making small angle approximations of $cos\theta \approx (1 - \theta^2/2)$ and $tan\theta \approx \theta$ and assuming the final contact angle $\theta_F \approx 0$ the following relation is obtained:

$$\frac{6\eta K_1 U}{\sigma_{LV}} = \theta^3. \tag{4.6}$$

The contact angle θ in Eq. (4.6) can be replaced by $4V/(\pi R^3)$ (where V is volume) with error less than 10% for angles $< 45°$ and U can be replaced by $\frac{dR}{dt}$. Eq. (4.6) can then be integrated to obtain:

$$R^{10} - {R_0}^{10} = A_1 t, \tag{4.7}$$

where $A_1 = 3\sigma_{LV}V^3/\eta K_1$ and R_0 is the initial radius of the spreading drop. By Eq. (4.2), this implies

$$A_{visc} = \pi \left[{R_0}^{10} + A_1 t\right]^{1/5}. \tag{4.8}$$

Taking the derivative of Eq. (4.8) with respect to time, the following relation is found for viscous spreading:

$$\frac{dA_{iner}}{dt} = \frac{\pi A_1}{5}\left[{R_0}^{10} + A_1 t\right]^{-4/5}. \tag{4.9}$$

4.2 Comparison of Inertial and Viscous Spreading Regimes

Area spreading rates in the inertial and viscous spreading regimes, described in Eq. (4.4) and Eq. (4.9), will be compared for EMI-BF_4 and EMI-IM at an arbitrary time of 10 seconds.

Consider EMI-BF_4 with values of $\sigma_{LV} = 0.052$ N/m, $\rho = 1294$ kg/m^3, $\eta = 0.0356$ Pa·s, a volume $V = 1$ μL, $R_0 = 10^{-3}$ m, and t = 10 s. These data give values of $dA_{iner}/dt = 2.51$ m^2/s and $dA_{visc}/dt = 5.33\times10^{-7}$ m^2/s suggesting that the inertial forces are quickly limited by the viscous effects.

Consider in a similar way EMI-IM, with values of $\sigma_{LV} = 0.0358$ N/m, $\rho = 1520$ kg/m^3, $\eta = 0.034$ Pa·s, and with the remainder of the values remaining the same as in the last paragraph. These values give $dA_{iner}/dt = 1.48$ m^2/s and $dA_{visc}/dt = 3.15\times10^{-7}$ m^2/s once again suggesting that the inertial forces are quickly limited by the viscous effects.

This result suggests that the experimental data should behave primarily according to the viscous spreading described by Eq. (4.8). Thus, a linear fit made with the area versus time data plotted on a log scale should have a slope of 0.2. However, in the third frame of Fig. (3-6), a halo of spreading fluid of a different thickness can clearly be seen around the central

spreading drop. It was also observed in experiment that the centralized portion of the drop within the halo reached a near constant radius within a minute or so of spreading. Thus, it is proposed that pressure builds up in the pores of the rough silicon surface and causes viscous spreading to reach a constant final contact angle and critical radius R_c while fluid continues to flow through the rough silicon surface like it might through a thin layer of a porous medium (see Fig. (4-3)). The critical radius R_c is the radius where the forces that were driving the viscous spreading of the central drop are balanced by the porous flow.

4.2.1 Porous spreading

The porous spreading regime occurs when pressure-driven fluid flow (provided by the bulk drop) spreads through the rough silicon surface opposed by viscosity.

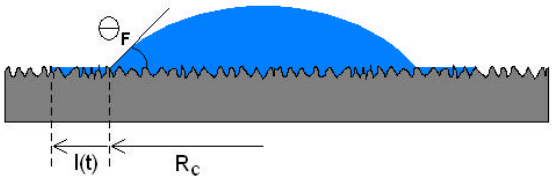

Figure 4-3: Illustration of fluid spread dominated by porous flow through the rough silicon surface.

To describe this flow, begin with the Poiseuille's equation for laminar flow, which states that

$$\frac{\Delta P}{l} = \frac{-32\eta u'}{D^2} \tag{4.10}$$

where ΔP is the pressure driving the porous flow provided by the bulk portion of the drop at a constant radius and contact angle, l is the length of the porous layer, u is the mean velocity through the pores, and D is the mean pore passage diameter. See Fig. 4-4 for illustration of porous flow.

Kozeny asserted that the volumetric flow rate through a porous layer must be equal to the mean flow rate through the actual open flow area.[15] This implies that the mean velocity through the pores u′ must be equal to the mean velocity through the entire porous layer u times a ratio of the cross sectional area of the porous layer to the cross sectional area of

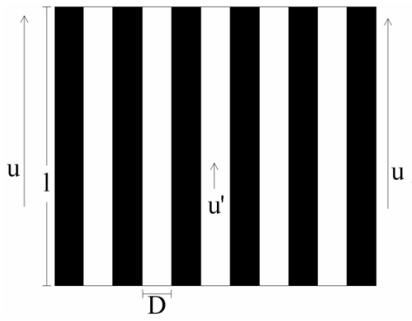

Figure 4-4: Cross-section illustration of flow through an ideal porous material with strait porous passages.

the flow path. The inverse of this ratio is known as porosity ε. Carman altered Kozeny's conclusion to include the importance of the ratio of actual channel length to the length of the porous layer in the following way:

$$u' = \frac{ul'}{\varepsilon l} \tag{4.11}$$

where l' is the mean length of the porous passages.[4]

By substituting Eq. (4.11) into Eq. (4.10) and assuming the mean velocity through the material is the derivative of the material length $u = \frac{dl}{dt}$ we get:

$$l\frac{dl}{dt} = \frac{-\Delta P \varepsilon D^2}{32\eta\,(l'/l)}. \tag{4.12}$$

Assuming the pressure driving the porous flow provided by the bulk portion of the drop ΔP is constant and the ratio of actual channel length to the length of the porous layer (l'/l) is constant, the resultant relation can be integrated to produce:

$$\frac{l^2}{2} = \frac{|\Delta P|\,\varepsilon D^2}{32\,(l'/l)\,\eta}t. \tag{4.13}$$

Solving for length l gives:

$$l = \sqrt{\frac{|\Delta P|\,\varepsilon D^2}{16\,(l'/l)\,\eta}t}. \tag{4.14}$$

Taking the derivative of Eq. (4.14) gives the following equation for velocity:

$$u = \frac{dl}{dt} = \sqrt{\frac{|\Delta P|\,\varepsilon D^2}{64\,(l'/l)\,\eta t}}. \tag{4.15}$$

Assuming the drop base area is circular the total spread area radius will be equal to the critical drop radius (radius where porous flow begins) plus the porous spread described in Eq. (4.14). Thus, we obtain a drop area due to porous flow of

$$A_{porous} = \pi \left(R_c + \sqrt{\frac{|\Delta P|\,\varepsilon D^2}{16\,(l'/l)\,\eta}} t^{1/2} \right)^2. \tag{4.16}$$

Taking the derivative of this relation with respect to time we find the following relation for porous spreading:

$$\frac{dA_{porous}}{dt} = \pi \left(R_c + \sqrt{\frac{|\Delta P|\,\varepsilon D^2}{16\,(l'/l)\,\eta}} t^{1/2} \right) \sqrt{\frac{|\Delta P|\,\varepsilon D^2}{16\,(l'/l)\,\eta}} t^{-1/2}. \tag{4.17}$$

4.2.2 Inertial and viscous spreading versus porous spreading

Assume EMI-BF_4 values and other values from section 4.2, $R_c = 5mm$, $|\Delta P| = 2.27 \times 10^4 N/m^2$ obtained from Eq. (4.14) with $t = 100$ s (a usual time where a ≈ 0.5 mm l values could be seen), $l = 0.5$ mm (which was a typical value seen in experiment at $t \approx 100$ s), $\varepsilon = 0.5$, $D = 500nm$ (the magnitude of the surface roughness height), and $l'/l = 2$. Substituting these values in to Eq. (4.17) results in $dA_{porous}/dt = 8.64 \times 10^{-8}$ m^2/s. Recall that for the same values for EMI-BF_4 in section 4.2, $dA_{iner}/dt = 2.2$ m^2/s and $dA_{visc}/dt = 3.23 \times 10^{-7}$ m^2/s suggesting that the inertial forces are quickly limited by the viscous effects which are then quickly limited by porous flow effects. This result agrees with the expected evolution of events.

Using the same values for $R_c = 5mm$, $|\Delta P| = 2.18 \times 10^4 N/m^2$ obtained from Eq. (4.14) with ε, D, t, l, and l'/l from the last paragraph, and EMI-IM values from section 4.2 results in $dA_{porous}/dt = 8.64 \times 10^{-8}$ m^2/s. Recall that for the same values for EMI-IM,

$dA_{iner}/dt = 1.48$ m^2/s and $dA_{visc}/dt = 3.15 \times 10^{-7}$ m^2/s suggesting that the inertial forces are quickly limited by the viscous effects which are then quickly limited by porous flow effects. This result also agrees with the expected evolution of events.

Chapter 5

Results

This chapter describes the results of the research. Results of the wetting measurements made are discussed. Results of the spreading rate experiments are presented and compared with the model presented in chapter 4. Important results of the thruster experiments are also presented. Finally, the black silicon treatment which was chosen as optimal is presented and discussed.

5.1 Wetting Measurement Results

Samples $2''$, $5'$, $8'$, $9'$, $10'$, $11'$, and $12'$ were chosen as good candidates for wettability based on surface roughness and contact angle measurements. All of these samples had high surface roughness measurements on the order of 500 - 900 nm except treatment $2''$ which had surface roughness less than 100's of nanometers. All samples had low near-zero contact angle measurements with EMI-BF_4 and EMI-IM propellants except treatment $9'$. Treatment $9'$ had an average contact angle of 11° for measurements done with EMI-BF_4. Thus, the roughest and most wettable of these samples were those with treatments $5'$, $8'$, $10'$, $11'$, and $12'$.

5.2 Spreading Rate Experiment Results

Spreading rate measurements of largest wetting radius (including thin porous layer spread) results are plotted in Fig. (5-1). Spreading experiments were performed several times for each black silicon sample to test for repeatability. Although sample 8′ had the largest roughness value, it had fairly average spreading. This contradiction could possibly be explained by the smooth spaces between the large peaks noted in the SEM images in section (3.3). It is also interesting to note that sample 2″ was the least rough sample and yet had an average spreading rate. Figure (5-1) shows that sample 10′ had the largest spreading rate. It can also be noted that spreading areas decreased after experiments were repeated on the same black silicon samples. This degradation of wettability is discussed further in section (5.3.2)

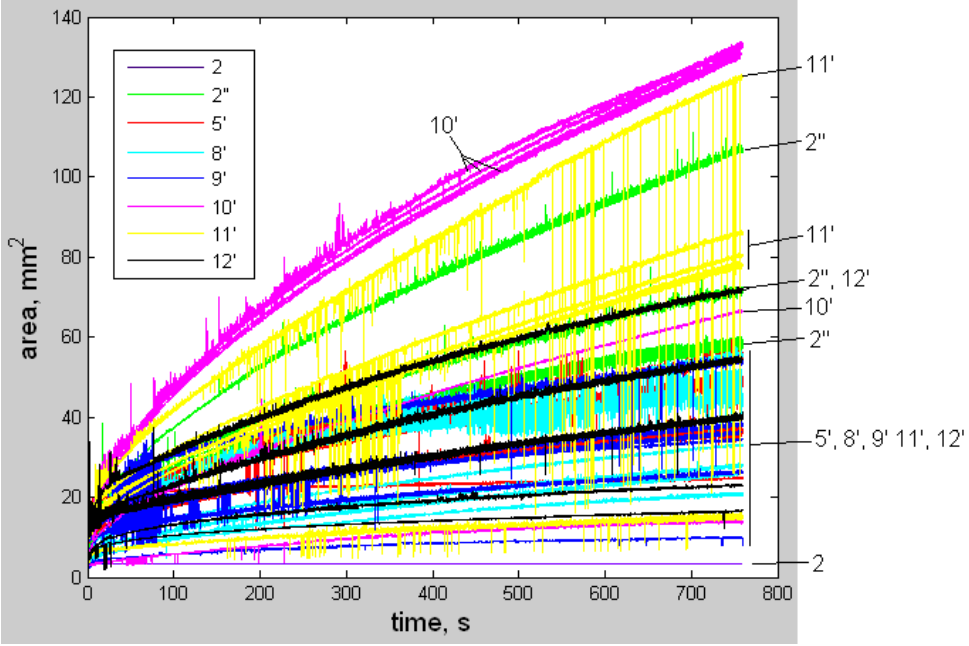

Figure 5-1: Plots of drop outermost spreading areas versus time for an μL drop on various black silicon samples. Samples 10′, 11′, and 2″ are the topmost curves indicating the largest spreading.

5.2.1 Spreading model comparison with experiment

For a perfectly smooth silicon substrate, spreading should be dominated by viscous forces (ignoring porous spreading). This behavior is described by Eq. (4.8). This suggests that a

linear fit made with the area versus time data plotted on a log scale should have a slope of 0.2. Actual spreading data (such as that shown in fig. 5-1) gave rise to log scale slopes ranging from 0.15 to 0.4 with an average of 0.33. Thus, experimental behavior loosely fits the viscous spreading model with a significant degree of error.

The porous spreading will give a curve fit of the form

$$A = \left(a + bt^{1/2}\right)^2 \tag{5.1}$$

was compared to the experimental data, where a and b are constant coefficients. From Eq. (4.17), it is expected that

$$a = \pi^{1/2} R_c \tag{5.2}$$

and

$$b = \sqrt{\frac{|\Delta P|\,\pi\varepsilon D^2}{16\,(l'/l)\,\eta}}. \tag{5.3}$$

Curve fits with data gave values of a ranging from 1.66×10^{-3} m to 4.86×10^{-3} m and values of b ranging from 2.15×10^{-5} m/s$^{1/2}$ to 3.08×10^{-4} m/s$^{1/2}$. Figure (5-2) shows the variation of the curve fit coefficients with the various data. There appears to be no obvious tend based on the variation of the samples.

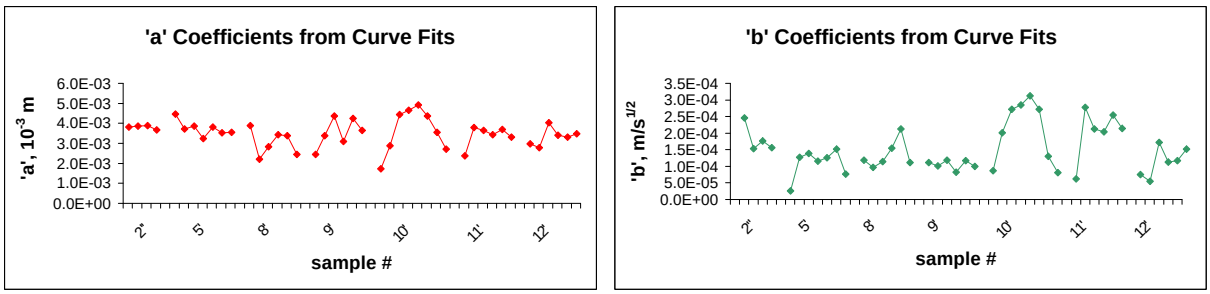

Figure 5-2: Plot of curve fit coefficients of spreading rate data.

The porous spread relation of area and time in Eq. (4.17) gave a much better fit with spreading data of largest drop area (including porous spreading layer) than the viscous spread relation provided by Eq. (4.8). This comparison of models is clearly seen in Fig. (5-3). The data fits gave root mean square errors ranging from 1.76×10^{-7} m^2 to 3.56×10^{-6} m^2 for drops areas on the order of $10 - 100 \times 10^{-5}$ m^2.

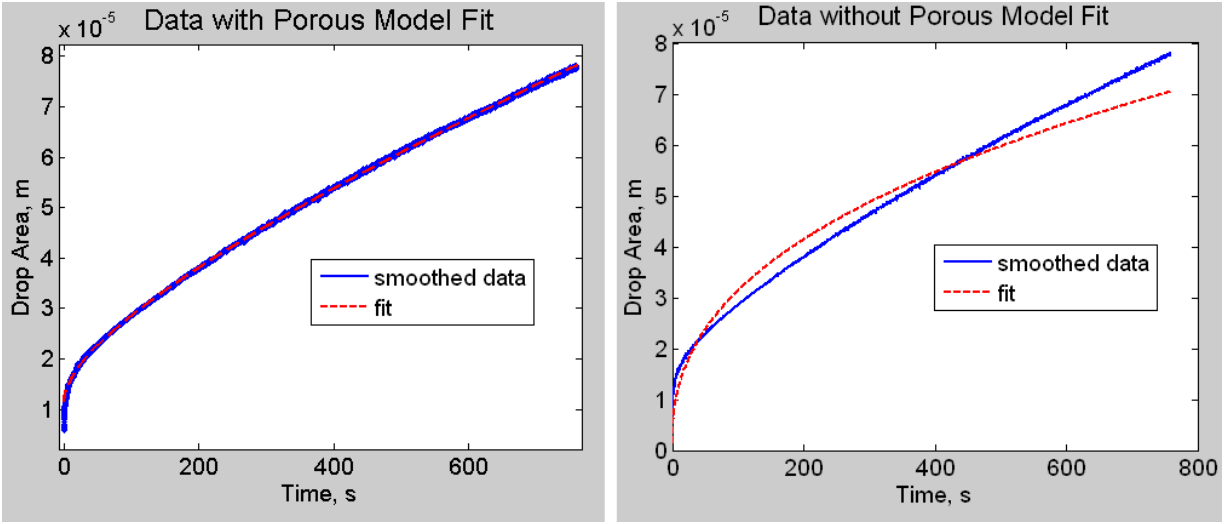

Figure 5-3: Sample of comparison of spreading rate data for EMI-BF_4 with model of porous spreading (left) and viscous spreading model (right). Although the left graph only shows one spreading sample and curve fit, the other curve fits were just as good with root mean square errors ranging from 1.76×10^{-7} m^2 to 3.56×10^{-6} m^2.

5.2.2 Order of magnitude calculation

For an order of magnitude approximation, assume $|\Delta P| = 2.27 \times 10^4 N/m^2$ obtained from Eq. (4.14) with $t = 100$ s (a usual time where a ≈ 0.5 mm l values could be seen), $l = 0.5$ mm (which was a typical value seen in experiment at $t \approx 100$ s), $\varepsilon = 0.5$, $D = 500nm$ (the magnitude of the surface roughness height), and $l'/l = 2$. Assume $\sigma_{LV} = 0.052$ N/m, $R_c = 5$ mm, and $\eta = 0.036$ Pa·s. This gives a coefficient a of the order 10^{-3} m and b of the order 10^{-4} m/s$^{1/2}$. The values obtained experimentally for a and b are the same order of magnitude as that estimated.

It would be desirable to perform the calculation in the last paragraph to bound the coefficient b with lower and upper estimates. We note that the coefficient a is only dependent on R_c which was observed experimentally not the vary greatly. Combining Eq. (4.14) with Eq. (5.3) we obtain:

$$b = \sqrt{\frac{\pi l^2}{t}}. \tag{5.4}$$

It was observed in experiment that l was near zero at t near zero and l was never bigger than maybe 1 mm for times no greater than 800 s. Thus the lower bound on b using these values would be 6.27×10^{-5} m/s$^{1/2}$ which is on the order 10^{-4} m/s$^{1/2}$ when rounded.

5.3 Thruster Experiment Results

5.3.1 Thruster performance

Treatments $2''$, $10'$, and $9'$ were chosen as likely candidates for producing favorable thruster performance. These treatments were applied to 4×4 emitter arrays and tested with the conditions outlined in chapter 2. Of the three, only sample $10'$ produced current. Current is not reported here because the data were only intended to measure thruster function. The experimental setup would need to be adjusted to get an accurate measure of current output. The extractor used for current measurement was fabricated with an error of hundreds of micrometers and alignment was done by eye. To obtain an accurate current measurement, a extractor should be microfabricated with the same accuracy and alignment as the thruster fabrication.

5.3.2 Wetting repeatability

Thrusters wetted well right after black silicon treatment were made. It was observed, however, that thruster wettability significantly decreased after the initially wetted thruster was cleaned with water for $\approx$ 10 minutes in an ultrasonic bath followed by a acetone clean for $\approx$ 10 minutes in an ultrasonic bath. Several cleaning processes were tried to alleviate this deterioration of wettability. First the cleaned chip was placed in a 10^{-7} Torr vacuum overnight in hopes that water trapped in the porous surface would evaporate and solve the wetting change. This attempt was unsuccessful. Secondly, the chip was placed in a oven at over 200° C in a few Torr atmosphere for a few hours in hopes of desorbing foreign matter that may have adhered to the surface. This process did not improve wettability either. Finally, a chip which had been wetted well before was cleaned with water for $\approx$ 10 minutes in an ultrasonic bath followed by a methanol clean for $\approx$ 10 minutes in an ultrasonic bath. This cleaning showed good results. The chip wetted well after cleaning although the wetting was not as fast as it had been before.

5.4 Black Silicon Treatments

Based on AFM imaging, SEM imaging, contact angle measurements, spreading rate experiments, and thruster current measurements, it has been determined that a black silicon plasma treatment with a 150 sccm Chlorine with 30 sccm Helium flow rates, a 50 mTorr chamber pressure, a 40 W bias power, and a 200 W source power produces a favorable silicon wettability and favorable performance on externally wetted microfabricated silicon electrospray thrusters. It was found that the treatment effectiveness depends on the conditions of the etching machine at the time of etch and the initial surface of the thruster. Etch time required to give good wetting varied from 9 minutes to 13 minutes in the treatments done on actual thrusters. The etch time needed to find an effective treatment thus must be found each time a group of black silicon treatment is done. The initial surface of the thruster will depend of its position on a wafer during previous fabrication steps. A few thrusters will have to be etched to guarantee an effective treatment is done on one.

Chapter 6

Conclusions and Recommendations

6.1 Review of Results

6.1.1 Spreading model and experimentation

This research has modeled the spread of propellant over a black silicon surface as a viscous spread which reaches a nearly constant critical radius and provides a constant capillary pressure source for porous flow through the black silicon surface for the remainder of the spreading. This model does a significantly better job of matching the kind of behavior seen in experiment than viscous spreading alone.

This model gives a relation that can be fitted within an average root mean square error of 8.72×10^{-7} m^2 for a spreading drop with an area of the order of 10^{-5} m^2. A number of questions are raised when attempting to account for the coefficients obtained by such a curve fit. These questions include:

1) What is an appropriate estimation for pore passage diameter for the surface roughness? It is unclear whether the liquid floods the surface roughness or stays at a height shorter than the surface roughness height.(See Fig. 6-1 for illustration.) It is also unclear whether the silicon surface geometry has feature separation comparable to the feature heights. These

uncertainties could account for disparities between the estimation for coefficients a and b and the experimental data in section 5.2.

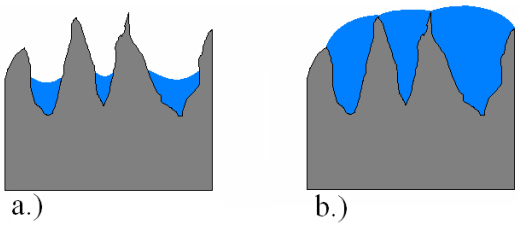

Figure 6-1: Illustration of potential variation in liquid height in porous surface.

2) Is the transition between spreading dominated by viscous forces and porous flow spreading gradual enough to warrant a solution found by an energy balance including both viscous and pressure flow terms? In chapter 4 it was assumed that spread dominated by viscous forces and porous flow spreading occurred independent of each other.

Another flaw with this model is that bulk drop internal pressure ΔP is assumed to be constant. This assumption implies that the bulk drop would not increase in area after reaching a critical radius R_c which was not observed in experiment. For a more accurate solution, one must consider how ΔP will vary with time. This would be done by understanding how the porous spreading communicates with the bulk drop which spread originally by viscously dominated spreading. Observation of experiment shows that the bulk drop front and porous spread front seem to alternate motion thus implying a communication between bulk drop and porous flow.

6.1.2 An optimal black silicon treatment

A black silicon plasma treatment with 150 sccm Chlorine with 30 sccm Helium flow rates, a 50 mTorr chamber pressure, a 40 W bias power, and a 200 W source power will produce favorable silicon wettability and favorable performance on externally wetted microfabricated silicon electrospray thrusters. In order to obtain a chip with good wetting, etch time must be found each time a group of black silicon treatments are done through trial and error. Also, a few thrusters with various initial surfaces will have to be etched to guarantee an effective treatment is done on one (although different chips can come from the same wafer).

Once a black silicon treatment had been applied to the thruster, a few steps will ensure good wettability of the thruster. First, the thruster should be wetted soon after the black silicon etch to prevent a large amount of surface oxidation. It is suggested that once a surface is wetted it should not be cleaned unless necessary. To clean a surface and ensure good wetting post cleaning one should clean with water for $\approx$ 10 minutes in an ultrasonic bath and follow this clean with a methanol clean for $\approx$ 10 minutes in an ultrasonic bath.

6.2 Future Fabrication

In the hopes of making a more repeatable silicon wettability treatment, it is suggested that work be done to find a process for producing black silicon that involves etching a patterned surface roughness. This could be done with an etch mask which would clearly define specific surface features instead of the random surface features created by the black silicon treatments. The work presented in this thesis was able to obtain a black silicon treatment which provided complete silicon surface wetting and thruster operation through trial and error. Black silicon formed by micromasking is a chaotic uncontrolled process which will always have questionable repeatability. Only by using a mask to define the black silicon features can a conclusive argument be made for why the silicon surface is wetting. Using a mask process will also allow investigators to have a basis for comparison between what is actually obtained from the etch process and what geometry is expected from the mask. This kind of comparison verification of wettable black silicon geometries can easily be done with a SEM. One problem that would arise with this kind of process is the resolution limitations of the photolithography used. The best resolution that can be obtained at MIT's Microsystems Technology Lab is around 1 μm. This kind of resolution is larger than the 600 nm typical protrusion sizes seen in this research. However, favorable wetting has been observed with black silicon roughness of this order in previous research.[31]

One must also consider emitter designs which encourage liquid flow to the sharp emitter tips. The smaller the radius of curvature a emitter tip has, the less likely it is that fluid will creep up it. Thus, the radius of curvature of the emitter tip and base must be carefully

designed so that large potentials will not be required to draw propellant to the places it needs to be.

Porous silicon is also a option for thruster surface wettability and propellant feed. Porous silicon can be achieved by a anodization process where a silicon wafer is used as the anode end of a electrical circuit in a solution of hydrofluoric acid and ethanol at tens to hundreds of $mA \cdot cm^{-2}$.[9] See figure 6-2 for an example of porous silicon made with anodization.

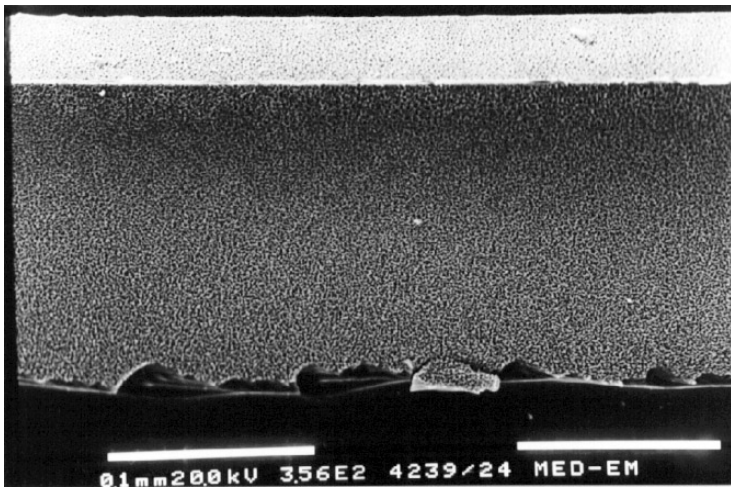

Figure 6-2: Porous silicon using anodization. Figure taken from Ref. [9].

The use of fabrication towards a surface that provides continuous fluid transport in the amount requested by the electric traction forces is an important next step in this research. This could be done with a porous silicon surface and tank backed by a constant pressure. This way flow through the thruster surface and propellant supply could be done with one design characteristic.

6.3 Future Theoretical and Experimental Work

Observing the drop spreading microscopically would be the next step in this research. It would allow questions mentioned in section 4.1 to be answered and for an even better model to be made.

There are a few steps that could be taken in understanding flow motion over electrospray

surfaces. The understanding of fluid spread over a dry substrate surface would help in understanding spread over a wetted substrate surface. Then flow over three dimensional wetted surfaces can be studied such as flow around corners and over tips. Next the flow in the presence of an electric field should be studied. This would mean understanding how the presence of an electric field changes the liquid and surface interface physics that would exist in the absence of an electric field. Finally, how this flow is affected by the liquid temperature might be studied to see how either heat application or cold temperatures could be beneficial or might negatively effect normal thruster operation.

Appendix A

Black Silicon Treatment Processes

Step	**Description**
Starting materials	DSP 6"(100) p-type silicon, 350 μm thick
1. Clean	- Piranha clean 10 minutes, greendot - TRL acid-hood or acid-hood2 (note: wafer becomes gold contaminated after this step)
2. Etch	- 25 m DRIE Si, recipe SF6-14 - TRL STS1 or STS2
3. Separate	- Saw into 20 mm 20 mm pieces - ICL diesaw
4. Clean	- 2 Piranha cleans 10 minutes, gold labware - TRL acid-hood
5. Mount	- place 20 mm $\times$ 20 mm piece on 4" handler wafer
6. Etch	- 0.5 m black silicon treatment, Cl2/N2 recipe, 1min to 25min - TRL plasmaquest
7. Dismount	- remove 20 mm $\times$ 20 mm piece from 4" handler wafer

Purpose of Process

The purpose of this process is to determine the optimum chemistry for producing a wettable black silicon treatment on DRIE silicon. After step 7, the surface roughness and wettability of the black silicon treated 20 mm $\times$ 20 mm piece will be analyzed under an atomic force microscope to find the surface roughness and with a contact angle goniometer to find the surface wettability. Processes 5. through 7. will be repeated with varied gas flow rates, pressures, and/or power levels in the step 6. etch recipe.

This black silicon wettability treatment is being developed for implementation in a process for creating electrospray thrusters. These electrospray thrusters utilize the capillarity effect

of liquid on the black silicon surface. The current electrospray thruster process involves steps in which gold contamination will be done before the black silicon treatment is made. Thus, it is necessary to find the optimum black silicon recipe in the gold contamination allowed machine.

Appendix B

Basic Sessile Drop Spreading Analysis Code

```
function [ ] = SpreadRate(read_fid, write_area_fid, write_perim_fid)


%SpreadRate.m - this program determines the surface area and
%perimeter covered by a 1 ul drop of EMI-BF4 or EMI-IM on a
%roughened silicon surface as a function of time from video images

clear

counter = 0;

for index = 1:2278
clear mov im map disk_size background ...
perc_gray bw dropdata bwdil bwdfill seD ...
bwfinal numObjects drop_area_prime drop_perim_prime
counter = counter + 1
%read drop spreading file
```

```
mov = aviread(read_fid, index);
%grab frames
[im, map] = frame2im(mov);
im = imrotate(im, 0);
%set colormap
colormap(map);
%crop
rect = [287 194 67 44];
im=imcrop(im,rect);

%put into grayscale
im = rgb2gray(im);
%imshow(im), figure
im = imadjust(im);
%imshow(im), figure
disk_size = 65;
background = imopen(im,strel('disk',disk_size));
set(gca,'ydir','reverse');
im = imadd(im,background);
%imshow(im), figure

%find image contours and dilate countours
perc_gray = 0.04;
bw = edge(im, 'sobel', (graythresh(im) * perc_gray));
se90 = strel('line', 3, 90);
se0 = strel('line', 3, 0);
bwdil = imdilate(bw, [se90 se0]);

%fill in object and smooth out edges
bwdfill = imfill(bwdil, 'holes');
seD = strel('diamond',1);
```

```
bwfinal = imerode(bwdfill,seD);
bwfinal = imerode(bwfinal,seD);
%imshow(bwfinal), figure

[labeled, numObjects] = bwlabel(bwdfill,4);
if numObjects ~= 1;
'Error: graythreshold to low. More than one object detected';
numObjects = numObjects;
end

%outline object
BWoutline = bwperim(bwfinal);
Segout = im;
Segout(BWoutline) = 255;
imshow(Segout);

%obtain data from image dropdata = regionprops(labeled,'Area', 'Perimeter');
for data1_index = 1:length(dropdata)
drop_area_prime(data1_index) = dropdata(data1_index).Area;
end
drop_area(counter) = max(drop_area_prime);
for data2_index = 1:length(dropdata)
drop_perim_prime(data2_index) = dropdata(data2_index).Perimeter;
end
drop_perim(counter) = max(drop_perim_prime);
end

drop_fid = fopen(write_area_fid, 'w');
for write1_index = 1:length(drop_area)
fprintf(drop_fid, '%7.0f\n', drop_area(write1_index));
end
```

```
fclose(drop_fid);
clear drop_fid
drop_fid = fopen(write_perim_fid, 'w');
for write2_index = 1:length(drop_perim)
fprintf(drop_fid, '%7.0f\n', drop_perim(write2_index));
end
fclose(drop_fid);
```

Bibliography

[1] Nano world: Black silicon for solar power. http://www.physorg.com, 2006.

[2] Tommaso Baldacchini, James E. Carey, Ming Zhou, and Eric Mazur. Superhydrophobic surfaces prepared by microstructuring of silicon using a femtosecond pulsed laser. *Langmuir*, 22(11):4917–4919, November 2006.

[3] James E. Carey, Catherine H. Crouch, Mengyan Shen, and Eric Mazur. Visible and near-infrared responsivity of femtosecond-laser microstructured silicon photodiodes. *Optics Letters*, 30(14):1773–1775, July 2005.

[4] P. C. Carman. Fluid flow through granular beds. *Transactions of the Institution of Chemical Engineers*, 15:150–166, 1937.

[5] Yu-Hui Chiu, Rainer A. Dressler, P. Terrence Murray, Paulo Lozano, and Manuel Martínez-Sánchez. Mass spectrometric analysis of ion emission for selected colloid thruster fuels. In *AIAA/ASME/SAE/ASEE 39th Joint Propulsion Conference and Exhibit*, Huntsville, AL, July 2003.

[6] E. Cohen and R. E. Kemp. Pulsed and alternating current colloid thruster studies. In *American Intitute of Aeronautic and Astronautics 8th Aerospace Sciences Meeting*, New York, NY, January 1970.

[7] P. G. de Gennes. Wetting: statics and dynamics. *Rev. Mod. Phys.*, 57(3):827–863, Jul 1985.

[8] Juan Fernández de La Mora and Ignacio González Loscertales. The current emitted by highly conducting taylor cones. *Journal of Fluid Mechanics*, 260:155–184, February 1994.

[9] Johan Drott, Kjell Lindstrm, Lars Rosengren, and Thomas Laurell. Journal of micromechanics and microengineering. *Journal of Micromechanics and Microengineering*, 7(1):14–23, 1997.

[10] Nicolas Eustathopoulos, Michael G. Nicholas, and Béatrice Drevet, editors. *De Magnete, Magneticisque Corporibus, et de Magno Magnete Tellure*. Physiologia Nova, London, 1600.

[11] Nicolas Eustathopoulos, Michael G. Nicholas, and Béatrice Drevet, editors. *Wettability at High Temperatures*, volume 3 of *Pergamon materials meries*. Pergamon, New York, 1999.

[12] J. V. Iribarne and B. A. Thomson. The journal of chemical physics. *On the evaporation of small ions from charged droplets*, 64(6):2271–2710, March 1976.

[13] Philip W. Kidd. Parametric studies with a single-needle colloid thruster. In *American Intitute of Aeronautic and Astronautics Electric Propuslion and Plasmadynamics Conference*, Colorado Springs, CO, September 1967.

[14] Philip W. Kidd. Research on the bipolar thrustor. *Air Force Aero Propulsion Laboratory Technical Report*, (110), September 1967.

[15] Josef Kozeny. *Über* kapillare leitung des wassers im boden. *Sitzungsbericht Wiener Akad. Der Wiss.*, 136:271–306, 1927.

[16] Paulo Lozano, Ben Glass, and Manuel Martínez-Sánchez. Performance characteristics of a linear ionic liquid electrospray thruster. In *Proceedings of the 29th Electric Propulsion Conference*, number 192, Princeton, NJ, November 2005.

[17] Paulo Lozano and Manuel Martínez-Sánchez. Ionic liquid ion sources: suppression of electrochemical reactions using voltage alternation. *Journal of Colloid and Interface Science*, 280(1):149–154, December 2004.

[18] Paulo Lozano and Manuel Martínez-Sánchez. Ionic liquid ion sources: Characterization of externally wetted emitters. *Journal of Colloid and Interface Science*, 282(2):415–421, February 2005.

[19] Manuel Martínez-Sánchez. 16.522 space propulsion. Massachusetts Institute of Technology OpenCourseWare, May 2005. Class Lecture.

[20] Manuel Martínez-Sánchez. Personal Correspondance, October 2006.

[21] Manuel Martínez-Sánchez and James E. Pollard. Spacecraft electric propulsion-an overview. *Journal of Propulsion and Power*, 14(5):688–699, 1998.

[22] Juergen Mueller. Thruster options for microspacecraft: A review and evaluation of existing hardware and emerging technologies. In *AIAA/ASME/SAE/ASEE 33rd Joint Propulsion Conference and Exhibit*, Seattle, WA, July 1997.

[23] Mark Paine. *Design Study for Microfabricated Colloidal Thrust.* MS dissertation, Massachusetts Institute of Technology, Department of Aeronautics and Astronautics, 1999.

[24] Julius Perel and John F. Mahoney. Interim report - mechanisms of emitter surface damage during ehd colloid particle generation and acceleration. *Air Force Aero Propulsion Laboratory Technical Report*, (0540).

[25] Julius Perel and John F. Mahoney. Micro-electric propulsion using charged clusters. In *9th Advanced Space Propulsion Workshop*, pages 355–363, March 1998.

[26] Julius Perel, R. David Moore, Arthur Y. Yahiku, and John Mahoney. Electrodeless particle thrustor. *Air Force Aero Propulsion Laboratory Technical Report*, October 1967.

[27] Ignacio Romero-Sanz, Rodrigo Bocanegra, Juan Fernández de La Mora, and Manuel Gamero-Casta no. Source of heavy molecular ions based on taylor cones of ionic liquids operating in the pure ion evaporation regime. *Journal of Applied Physic*, 94(6):3599–3605, September 2003.

[28] S. Singer and M. Farber. Electro-propulsion with colloids. *Astronautics*, 1962.

[29] K. W. Stark and A. Sherman. Present status of colloid microthruster technology. *NASA Technical Note*, (D-5305), 1968.

[30] Geoffrey Ingram Taylor. Distintegration of water drops in an electric field. *Proc. R. Soc. London A*, 280(1382):383–397, 1964.

[31] Luis F. Velásquez-García. *The Design, Fabrication and Testing of Micro-fabricated Linear and Planar Colloid Thruster Arrays*. PhD dissertation, Massachusetts Institute of Technology, Department of Aeronautics and Astronautics, 2004.

[32] Stanley H. Wineland and Robert E. Hunter. Negatively charged colloid generation research. In *American Intitute of Aeronautic and Astronautics 5th Electric Propuslion Conference*, number 66.

[33] S. Zafran. Colloid advanced development program. *NASA Technical Report*, (14009), 1977.